Thermal conductivity and secondary porosity of single anatase TiO$_2$ nanowire

Xuhui Feng, Xiaopeng Huang and Xinwei Wang

Department of Mechanical Engineering, 2010 Black Engineering Building, Iowa State University, Ames, IA 50011, USA

E-mail: xwang3@iastate.edu

Abstract

Single anatase TiO$_2$ nanowire is synthesized using the electrospinning technique with the sol–gel method and is suspended over a pre-processed 100 μm-wide TEM grid for further characterization. The diameters of the nanowires fall in the range of 250–400 nm. The transient electrothermal (TET) method is adopted to acquire the voltage–time (U–t) profile of the Ir-coated nanowire under step Joule heating. The intrinsic thermal diffusivity of single anatase TiO$_2$ nanowires varies from 1.3 to 4.6 $\times$ 10^{-6} m^2 s^{-1}, and the thermal conductivity changes distinctly from 1.3 to 5.6 W m^{-1} K^{-1}, much lower than the value of the bulk counterpart: 8.5 W m^{-1} K^{-1}. The density and thermal conductivity increase significantly with the diameter, largely because at larger diameters less secondary porosity is left by decomposition of organic composites and their escape from the wire during calcination. The density of TiO$_2$ nanowires is found to be much lower than that of the bulk counterpart. This is supported by the SEM image of the secondary porous surface. High secondary porosity is observed for TiO$_2$ nanowires, ranging from 18% to 63%. This very high secondary porosity confirms that the decomposition of PVP content may distort the fibrous matrix and leave vacancies. In addition, the transition from amorphous to anatase phase could also create a porous state due to crystal particle aggregation.

(Some figures may appear in colour only in the online journal)

1. Introduction

Low-dimensional structures, including nanoscale films and wires/fibers/tubes, have demonstrated their intriguing novelties and promising applications in the electronic, optical, energy and micromechanical industries [1]. As an important nanomaterial whose properties are significantly affected by dimensionality [2], low-dimensional nanostructures of titanium dioxide (TiO$_2$) have been attracting considerable attention from both fundamental and practical perspectives when the particle size, crystalline state and morphology are altered [3, 4]. TiO$_2$-based catalyst was first commercially applied in the 1970s for air pollution control equipment [5]. More intensive and in-depth applications of TiO$_2$ materials can also be found in photocatalytic decontamination [6], sensor materials [7, 8], dye-sensitized solar cells [9] and photoelectrochemical cells [10]. A variety of techniques have been employed for synthesizing TiO$_2$ nanostructures, such as

the sol–gel method [11–14], hydrothermal reaction [15–21], anodic oxidation [22–26], electrospinning [27–31], and many others [32–41]. The properties of TiO$_2$ nanostructures vary substantially with the synthesis method [42] and large collections of studies and achievements have been reported regarding their electrical and thermal properties and how they are influenced by various TiO$_2$ nanostructures. Berman and Forster [43] conducted measurements on the thermal conductivity of several dielectric crystals including TiO$_2$ rutile. They concluded that limitations in the isotopic species of the chemical elements in the crystal caused it to behave differently from the Peierls predicted thermal conductivity curve for perfect crystals. Matsuda [5] found that the thermal stability limit temperature of TiO$_2$ is around 700–800 °C since sintering is accomplished by crystalline transition from anatase to rutile at about 700 °C. For utilization in dye-sensitized solar cells, TiO$_2$ nanowires were treated with Nb(Oet)$_5$ solutions and it was confirmed in Beppu's

work [44] that they have high heat resistant properties and a distinct fiber shape when heated up to 450 °C, which consequently increases the electron diffusion coefficient and photoelectrical conversion efficiency. Lambropoulos [45] measured the thermal conductivity of TiO_2 thin films and the results demonstrated that with a silicon substrate, TiO_2 thin film has a thermal conductivity lower than the bulk value by more than one order of magnitude. Wu *et al* [46] studied the thermal conductivity of electron-beam- (EB-) deposited and ion-plated (IP) thin films of TiO_2. The properties of EB-deposited and IP processed TiO_2 are 0.25 and 0.45 W m^{-1} K^{-1}, respectively. Lee's work [47] indicated that for sputtered TiO_2 thin films, the thermal conductivity is highly dependent on the substrate temperature since the substrate temperature strongly influences the grain size and also decreases the density of atomic-scale defects. The cross-plane thermal conductivities of highly ordered amorphous and crystalline mesoporous TiO_2 thin films were measured for porosities of 30% and 35% [58]. The thermal conductivity of crystalline sol–gel mesoporous TiO_2 thin film was found to be about 1.06 W m^{-1} K^{-1} and a comparison was made to show that the connectivity and size of the crystalline domains can provide control over the thermal conductivity in addition to the porosity. These investigations on various forms of TiO_2 material lead to a conclusion that the thermal properties of TiO_2 materials are strongly related to the crystalline morphology, mesoscopic structure and macroscopic form.

Although intensive attention has been devoted to studies of TiO_2 nanostructures, most work concentrates on nanofilms and nanowire arrays, both of which contain numerous nanowires and nanofibers, and no results have been presented concerning the thermophysical properties of single TiO_2 nanowire. The way in which the polymorph structure of single TiO_2 nanowire affects its thermal performance remains uninvestigated. Additionally, as a crucial physical property, the density has drawn little attention when TiO_2 emerges in different forms and structures. To fulfil these purposes, in this work single anatase TiO_2 nanowire is synthesized using the electrospinning method and investigated using the transient electrothermal (TET) technique [48] characterization combined with a calibration procedure to understand the thermophysical properties and porosity in this specific crystalline structure. In previous work [49] we employed the TET technique to investigate the thermal conductivity of thin films composed of TiO_2 nanofibers and the value was found to be much lower than that of a dense state. Modifications are made to make the TET technique and calibration procedure more specifically suitable for the samples in this study and are presented in section 2. Thermal property analysis and discussion of the secondary porosity are included in section 3.

2. Experimental details

2.1. Anatase TiO_2 nanowire fabrication

Because of the extremely small scale, preparation of single TiO_2 nanowires requires very delicate and complicated

processes. Figure 1 presents the whole sample preparation procedure including the electrospinning technique setup, the coating of iridium film over the nanowire, the focused ion beam- (FIB-) assisted platinum soldering process and the final configuration of the testing device. In order to synthesize parallel TiO_2 nanowires for further manipulation and characterization, the electrospinning technique, as a manageable and efficient technique to synthesize fibular nanostructures, is employed in this work and the experimental setup is indicated in figure 1(a). 1.5 g of titanium tetraisopropoxide (Ti(O*i*Pr)$_4$, from Aldrich) was mixed with 3 ml of ethanol and 3 ml of acetic acid in a beaker. After 10 min the mixture was moved into 7.5 ml of ethanol that contained 4.5 g of poly(vinyl pyrrolidone) (PVP, Aldrich, Mw 1300 000), followed by magnetic stirring in a capped vial. The well-stirred solution was immediately transferred into a syringe that was equipped with a 23-gauge stainless-steel needle. The needle tip was connected to a 20 kV ultra-high voltage source. A piece of transmission electron microscopy (TEM) grid with two 1.5 mm × 0.1 mm slots was pre-coated with gold to make only one slot nonconductively open and was then positioned about 8–10 cm below the needle. The two slots acted as symmetric collectors to create a symmetric electrical force to collect highly oriented nanowires. With a symmetric ultra-high electric field of about 2 kV cm^{-1}, the polymer solution was ejected from the needle tip, stretched into continuous ultrathin wires and then deposited with a highly oriented alignment [50]. The as-spun nanowires were then placed in open air for 5 h to achieve complete hydrolysis, followed by 3 h of calcination at 500 °C to remove the PVP content. During calcination, size reduction was observed as mentioned in our previous work because of the decomposition of PVP content [49]. This process potentially causes internal structure irregularities and defects, inducing certain impacts on the material properties. After selective removal of the other nanowires with tweezers, only one nanowire was left over the slot for later processing and characterization, as presented by the TEM grid in figure 1(b). A slight modification from our previous experiment is that iridium sputter coating was applied in this work (by a Q150T sputter coater) over the TiO_2 nanowire for electrical conducting purposes, instead of gold coating [49]. Gold film is prone to a 'micro-island' effect, causing a rough coated film surface and probably a poor electrical contact when the sample is relatively small. Comparatively, iridium film is known to be much finer and more uniform than gold film and it improves the coating uniformity and conducting effect significantly. In this work, the thickness of the iridium coating was roughly 15 nm and the consequent resistance was controlled from a few thousand ohms to tens of thousands of ohms. The physical and mathematical interpretation of the iridium film effect will be introduced in section 3. Because the nanowire was simply suspended over the TEM grid slot, the contact between the nanowire and the grid surface might not be good enough to eliminate/suppress the influence of contact thermal/electrical resistance. Focused ion beam-assisted platinum soldering (Quanta 3D Dual-beam system) was used to weld both ends of the nanowire to the TEM grid surface. As seen in the right
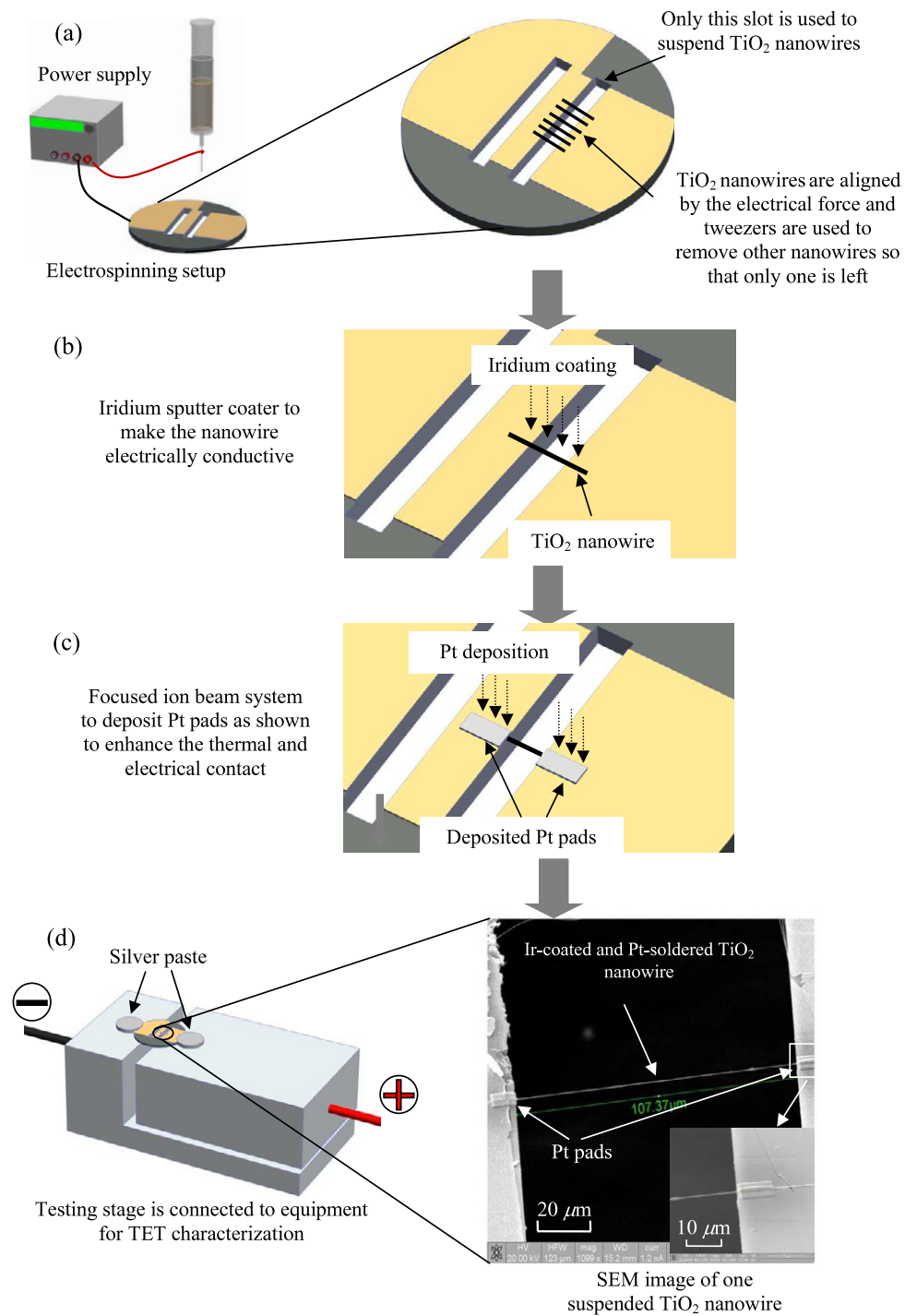
Figure 1. The complete sample preparation procedure includes the following processes. (a) An electrospinning experiment to fabricate parallel TiO$_2$ nanowires. On the right is a magnified image of a TET grid for suspending deposited parallel samples. (b) An iridium sputter coater for sputter coating a thin iridium film over the single TiO$_2$ nanowire; on the right is a magnified picture of the working slot only. (c) A focused ion beam-assisted platinum soldering process to solder both ends for the purpose of better electrical and thermal conduction. Two soldered Pt pads are shown to cover both ends of the nanowire on the slot in the right image, (d) The whole piece of TEM grid with Ir-coated and Pt-soldered TiO$_2$ nanowire is transferred onto a testing stage for further thermal characterization. On the right is an SEM image of the fully prepared TiO$_2$ nanowire, which is marked as sample 7 in this experiment.

image of figure 1(c), both ends of a single TiO$_2$ nanowire are covered by deposited rectangular-shaped Pt pads. In figure 1(d), the left image gives the overall configuration of a testing base with the prepared TEM grid and suspended Ir-coated and Pt-soldered TiO$_2$ nanowire. This testing base

was then moved into a vacuum chamber for further thermal characterization. As discussed before, due to the extremely low pressure, convective heat transfer is minimized. For the radiation heat transfer, our previous work has provided detailed analysis about its impact in the TET experiment [57].
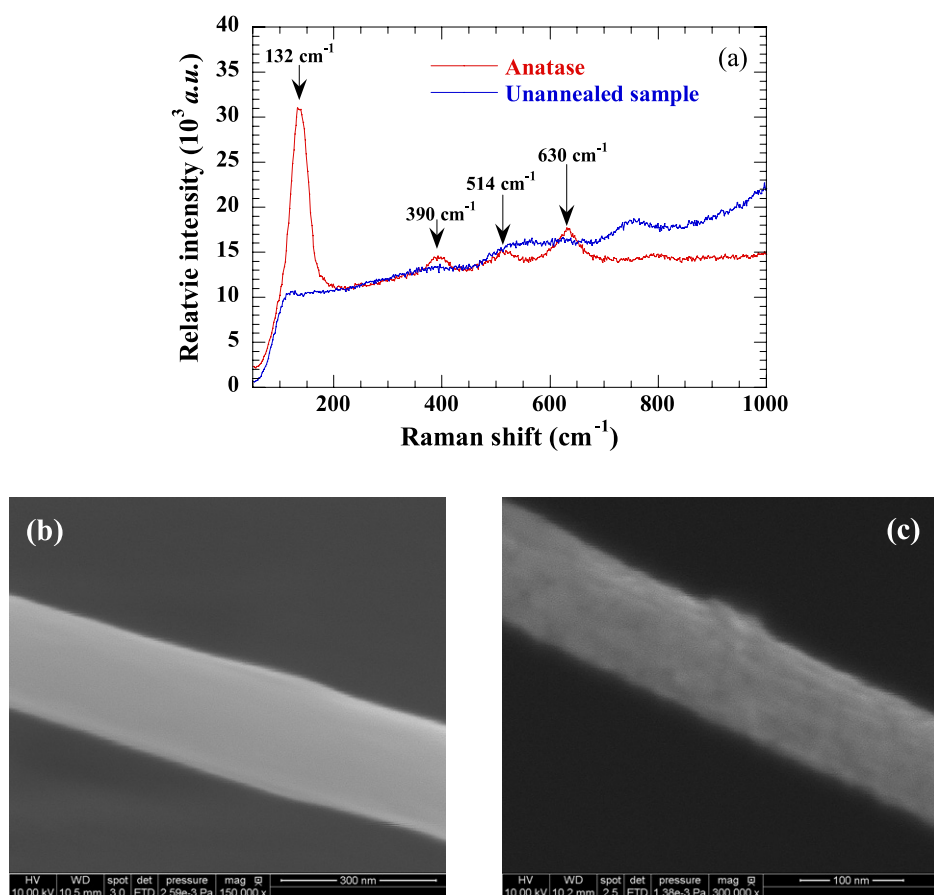
Figure 2. (a) Raman spectra of a TiO$_2$ nanowire after complete calcination to confirm its anatase polymorph, compared with the Raman spectra of an unannealed sample. (b) High-magnification SEM image at 150 000× of the as-spun nanowire to show that the surface is very smooth. (c) SEM image at 300 000× magnification of a calcinated TiO$_2$ nanowire that enhances the bumpy and porous surface. The images in (b) and (c) are not from the same sample and are only for surface porosity demonstration purposes.

For the samples measured in this work, our analysis shows the amount of radiation heat transfer from the nanowire is about 2% or less when compared with Joule heating in the sample. Therefore, the major mechanism to transfer the thermal energy is conductive heat transfer. On the right of the figure is the scanning electron microscopy (SEM) picture of nanowire sample 7 and two Pt pads are clearly seen on both ends of the nanowire with an enlarged inset picture of one pad. This pad completely covers the nanowire–base contact and ensures excellent electrical conduction and heat dissipation.

To confirm the polymorph of the prepared sample, examination of the Raman spectra is conducted using a Voyage confocal Raman spectroscope. Raman spectra of TiO$_2$ nanowires are displayed in figure 2(a) to show the authenticity of the anatase crystal structure. Four distinct peaks at 132, 390, 514 and 630 cm^{-1} show that the annealing at 500 °C for 3 h has turned the amorphous material into anatase crystalline material, which is consistent with previous discussions [49]. Raman spectra of unannealed amorphous TiO$_2$ nanowires are also presented in this figure for comparison. According to Ohsaka *et al* [51], the peaks at 132 and 390 cm^{-1} are the O–Ti–O bending-type vibrations, and the other two peaks at 514 and 630 cm^{-1} represent the Ti–O bond stretching-type vibrations. Additionally, in

order to observe the impact of the calcination and also the surface structure of the nanowire, SEM is employed to investigate the nanostructure. In figure 2(b), the sample is obtained simply after hydrolysis in open air for 5 h and the surface structure is very smooth with no dents or other features evident. Figure 2(c) presents an image of a calcinated nanowire which exhibits a wavy and uneven surface structure. Similar phenomena have been generally observed in electro-spun TiO$_2$ nanofibers [50, 27, 29, 31]. The porous structure existing between the nanofibers inside the bulk material is called the primary porous structure. The porous structure within individual TiO$_2$ nanofibers occupies a relatively smaller portion and exists in smaller scale. Therefore, it is defined as the secondary porous structure for comparison purposes [27]. The way in which it originates can be interpreted as follows. First, the TiO$_2$ nanowires are sintered by aggregation of TiO$_2$ particles with continuous crystallization at a high temperature because the particles favor a round shape to minimize the surface area. Second, the decomposition of PVP content during calcination distorts the nanowire and leaves an irregular fibrous matrix along with shrinkage of the nanowire diameter. Consequent internal structure irregularity and imperfections from calcination will
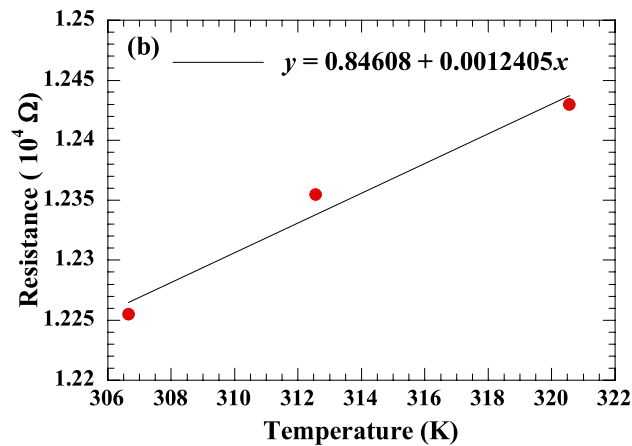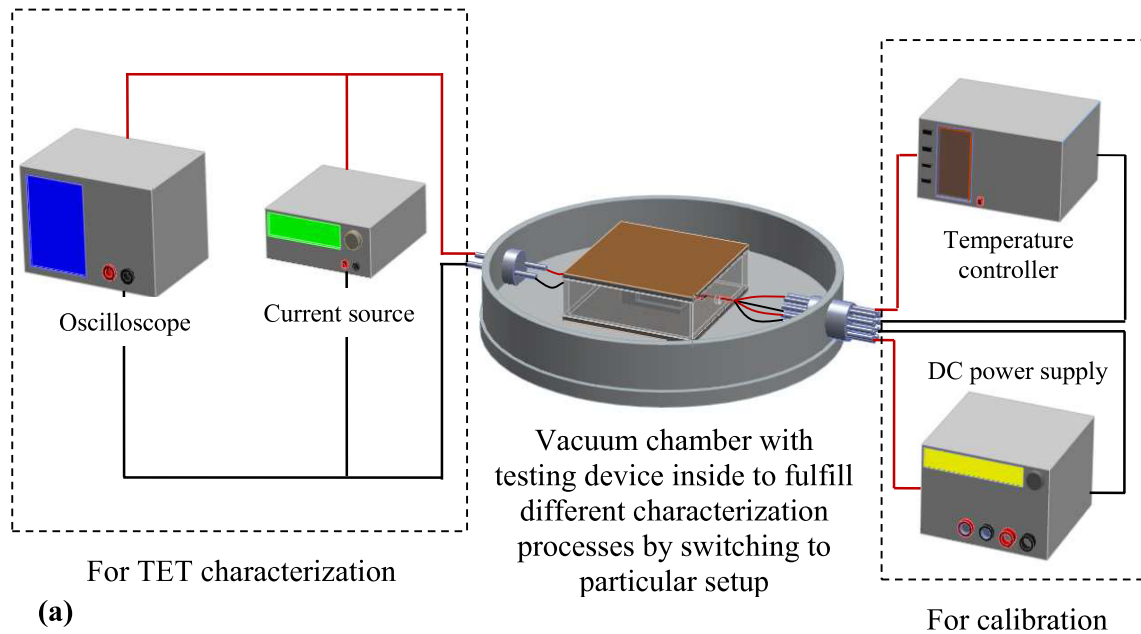
Figure 3. (a) Schematic of the thermal property characterization setup. A testing device is positioned in a vacuum chamber that is connected to two equipment sets. The left dashed box shows the equipment for TET characterization and the right dashed box shows the equipment for the calibration experiment. (b) A fitted linear profile of sample 7 from the calibration experiment for determining the temperature coefficient of resistance.

be the principal explanations for the dramatic change of physical properties and thermal performance.

2.2. TET measurement

The prepared testing base shown in figure 1(d) is ready for thermal characterization. Both the electrical and the thermal conductance of TiO_2 nanowires are dramatically enhanced by the iridium coating and they therefore show metal-like characteristics. To determine the temperature coefficient of resistance of a TiO_2 nanowire, a calibration procedure is performed in a vacuum chamber and the configuration is indicated in the right dashed box in figure 3(a). Unlike previous microscale film-like samples [49], it is difficult to directly apply thermocouples to the nanowire surface to sense the temperature change due to the nanometer scale. Furthermore, the layered structure at the wire–base

contact generated in the sample preparation will cause significant thermal dissipation among layers, thus the ambient temperature will be most likely different from the temperature of the sample. In order to accurately monitor the temperature change of the sample, a device is designed and placed in the vacuum chamber (figure 3(a)) to both create a uniform temperature field and maintain thermal equilibrium between the sample and the ambient conditions. For the testing device, the distance between the top and bottom plates is about 1 inch and both plates are covered with Kapton insulated flexible heaters (from Omega) as the heat sources. The wall is made of acrylic glass to reduce unnecessary heat loss. This testing device positioned in the vacuum chamber in figure 3(a) along with the equipment in the right dashed box is specifically designed for the calibration procedure. Adjustable DC power for both heaters is provided by a dual-output DC power supply (Agilent E3649A) and two pasted thermocouples

are connected to a programmable temperature controller (Stanford Research Systems) to monitor the temperature through the whole calibration process. The calibration process is performed when the temperature descends from about 50 °C to room temperature. During the cooling process, limited power is provided from the power supply to ensure that the whole process is slow and moderate so that the assumption of quasi-equilibrium is appropriate to describe this calibration procedure. Taking sample 7 for instance, its typical calibration curve is shown in figure 3(b), in which the resistance reduces from about 12 440 to 12 250 Ω while the temperature decreases from 321 to 307 K. Linear fitting is established based on the recorded data and the deviation from standard metal-like resistance–temperature properties is probably attributed to the structure of the Ir on the nanowire surface. The fitted temperature coefficient of resistance for sample 7 is about 12.4 Ω K^{-1} and it is adopted to evaluate the temperature change during the transient heating process. This temperature change could eventually be applied to calculate the effective thermal conductivity of the nanowire. To measure the thermal diffusivity, TET characterization is also performed when the testing base is placed in the same device while the measurement is switched to another setup shown in the left box in figure 3(a). A current source (Keithley 6221) is connected to the testing base to supply a step current and an oscilloscope (Tektronix TDS 7054 digital phosphor oscilloscope) is employed to monitor and record the induced real-time voltage–time (*U*–*t*) profiles. The current should be controlled to provide a response that is strong enough to be captured and analyzed but also to keep the sample structure intact. Meanwhile, the frequency must also be appropriate to have a useful profile that contains both rising state and steady state.

3. Results and discussion

3.1. Physical model of the TET technique

The effectiveness of the TET technique for measuring the thermal properties of conductive, semi-conductive and even nonconductive materials has been introduced in previous work [48, 49]. With an appropriately coated conductive layer, semi-conductive and nonconductive wires exhibit distinct electrical conductive properties and provide signals strong enough for detection. A schematic of the TET experimental setup is shown in the left dashed box in figure 3(a). The sample is housed in a vacuum chamber whose pressure is below 10^{-3} Torr to suppress heat convection to a negligible level. Meanwhile, the heat transfer by radiation is also negligible from previous discussion [57]. The physical model of the TET technique is developed based on one-dimensional heat conduction theory [49]. The electric heating q_0 is assumed constant and both ends of the sample are considered to have constant temperature since the aluminum stage is large enough to dissipate the heat compared with the size of the sample. When the convection effect is negligible under 1 mTorr, the governing equation is expressed as

$$\frac{\partial(\rho c_p T)}{\partial t} = k\frac{\partial^2 T}{\partial x^2} + q_0, \tag{1}$$

where ρ, c_p and k are the density, specific heat and thermal conductivity of the sample, respectively. The detailed procedure to solve this governing equation is given in Guo's work [48]. Only the expression of the temperature distribution is presented here for further analysis purposes,

$$T(t) = \frac{1}{L}\int_{x=0}^{L} T(x,t)\,\mathrm{d}x = T_0 + \frac{8q_0 L^2}{k\pi^4}$$
$$\times \sum_{m=1}^{\infty} \frac{1 - \exp[-(2m-1)^2\pi^2\alpha t/L^2]}{(2m-1)^4}. \tag{2}$$

When the temperature distribution along the sample reaches the steady state, the average temperature of the wire becomes $T_0 + q_0 L^2/(12k)$. q_0 is the electrical heating power per unit volume and can be expressed as $q_0 = Q/(LA) = I^2 R/(LA)$, while Q is the electrical heating power and A and L are the cross-sectional area and length of the sample, respectively. With the calibration result for the temperature coefficient of resistance η and the resistance change ΔR during the heating process, the temperature change $\Delta T = T_{\text{steady}} - T_0$ is calculated and then the thermal conductivity is obtained as $k = QL/(12A\Delta T)$. Meanwhile, the dimensionless temperature increase is written as

$$T^* = \frac{96}{\pi^4}\sum_{m=1}^{\infty} \frac{1 - \exp[-(2m-1)^2\pi^2\alpha t/L^2]}{(2m-1)^4}. \tag{3}$$

The voltage evolution (U_{sample}) recorded by the oscilloscope is directly related to the average temperature change of the sample as

$$U_{\text{sample}} = IR_0 + I\eta\frac{8q_0 L^2}{k\pi^4}$$
$$\times \sum_{m=1}^{\infty} \frac{1 - \exp[-(2m-1)^2\pi^2\alpha t/L^2]}{(2m-1)^4}, \tag{4}$$

where U_{sample} is the voltage over the sample recorded by the oscilloscope, I is the constant current fed through the sample and R_0 is the resistance of the sample without heating. It is important to observe that the measured voltage change (equation (4)) and the normalized temperature change (equation (3)) share an identical term, in which the thermal diffusivity is contained. In our work, first we obtain the normalized temperature rise based on the measured U–t profile. Then theoretical prediction is conducted using equation (3) based on a guessed thermal diffusivity and is compared with the experimental result. The value of thermal diffusivity giving the best fit (least squares method) of the experimental result is taken as the thermal diffusivity of the sample. In this work, the TET characterization is conducted at two or three different current levels for each sample to reduce possible noise and uncertainty from the equipment and environment.

3.2. Data processing in TET measurement

As seen in figure 4, when a step DC current provided by the current source is fed through the nanowire, a quick response of voltage evolution of the nanowire is

detected by the high-speed oscilloscope. Because of the layer-like configuration at the wire–base contact generated by the sample preparation, an undesired effect such as capacitance may be included and cause deviation from a pure temperature–resistance relationship. Normally, only one U–t profile is required for data fitting to determine the thermal diffusivity. To exclude unnecessary effects, two U–t profiles of sample 7 at different feeding currents are needed, as shown in figure 4(a). Two profiles at 20 and 10 μA are plotted out and the ratio of their voltage responses is also presented in the same figure. After precisely calculating the voltage increase, it was found that the voltage is not proportional to the resistance during the transient state, indicating that the nanowire's transient response is nonlinear and other effects might be included as mentioned before. To exclude other unnecessary effects, the acquired ratio profile will be used for the data fitting process because, after this treatment, irrelevant effects can be significantly reduced and it largely contains the R–t relation. In addition, because of the Joule heating, the electrical heating power Q is not constant any more. Therefore, to precisely obtain the effective thermal diffusivity, numerical simulation with varying heat source $Q(t)$ is employed based on the one-dimensional heat transfer model. The average temperature of the whole sample within each time interval is calculated to obtain the temperature–time profile until steady state is reached. By changing the thermal diffusivity and repeating the numerical procedure, the thermal diffusivity giving the best fit is considered as the thermal diffusivity of the sample. Detailed theoretical analysis of this signal processing will be discussed in another work. A fitted curve is shown in figure 4(b) and it is observed that the fitted normalized curve is very consistent with the theoretical one, indicating that the obtained effective thermal diffusivity is accurate enough. The fitted value for sample 7 is 2.1×10^{-6} m^2 s^{-1}, which is acceptably close to the literature value of 3.2×10^{-6} m^2 s^{-1} [52, 53], considering measurement uncertainty and possible interior structural defects and vacancies that may have emerged from the fabrication. Another two theoretical profiles based on thermal diffusivities of 2.3 and 2.0×10^{-6} m^2 s^{-1} are also presented in figure 4(b) to demonstrate the fitting sensitivity. The fitting uncertainty is determined by varying the thermal diffusivity slightly until distinct deviation is observed between the theoretical prediction and the experimental results. The uncertainty in the fitting procedure of thermal diffusivity determination for this sample is about 8%, which will be considered in the uncertainty analysis.

The approach to determining thermal conductivity is modified as well as compared with our previous work [49] and a demonstration will be presented with sample 7 as the example. For the TET measurement at each temperature, various currents are supplied to acquire different profiles. For instance, for sample 7 indicated in figure 4, four different currents, 10, 20, 30 and 40 μA, are applied to the sample at 51 °C and the profile under each current is recorded individually. As a metal-like material, the voltage at steady state ascends with increasing current. Based on the TET theory, the thermal conductivity is determined
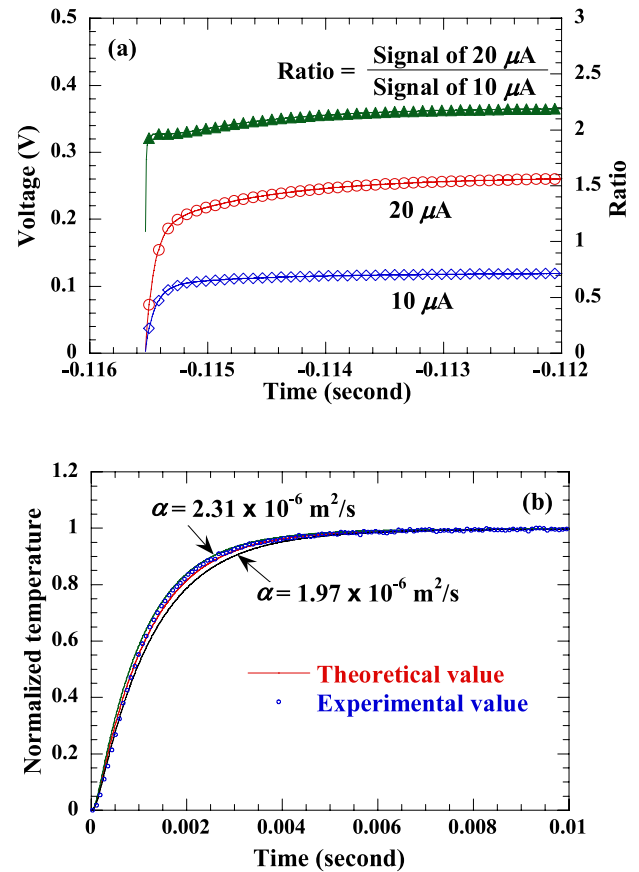
Figure 4. (a) U–t feedbacks of 10 and 20 μA current feeds for sample 7; the solid line with triangles represents the ratio of the two U–t profiles. (b) Comparison plot between the theoretical results and experimental fitting for sample 7, with another two fitting curves to demonstrate the uncertainty of this fitting process.

as $k = QL/(12A\Delta T)$. From the calibration results, the temperature difference is substituted by the resistance change to modify the equation to $k = QL\eta/(12A\Delta R)$, where η is the temperature coefficient of resistance. Therefore the linear relationship between steady state resistance and supplied power is derived to be $\Delta R/Q = L\eta/(12kA)$, and this relationship for sample 7 is shown in figure 5, demonstrating an excellent linear trend. A linear fitting is also exhibited in the same figure and the obtained slope contains the thermal conductivity when other parameters are known. For this sample, the slope of the fitted straight line is calculated as 3.08×10^8 Ω W^{-1}. After incorporating other parameters such as sample length L, cross-sectional area A and measured temperature coefficient of resistance η, the effective thermal conductivity of sample 7 is finally determined as 4.1 W m^{-1} K^{-1}, which still includes the impact from the iridium coating and will be modified to eliminate this influence. In this methodology, the cross-sectional area A is calculated from only the diameter of the bare TiO$_2$ nanowire. Although the thickness of the iridium coating is only about 15 nm, which is extremely small compared with the nanowire diameter of about 300 nm, it is more appropriate and accurate to include this thickness in the cross-sectional area evaluation. Because of the coating principle, the coated iridium film
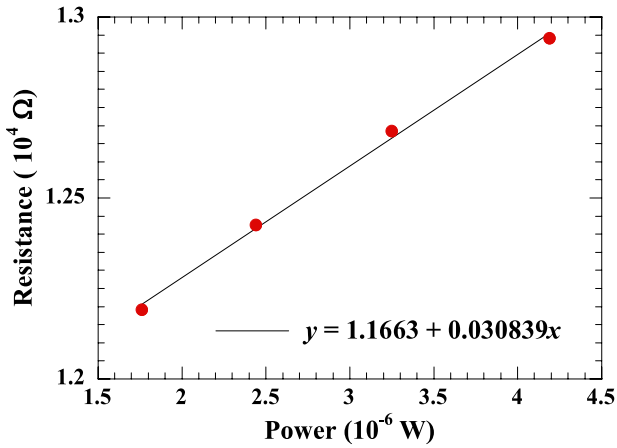
Figure 5. Linear relationship between the resistance at steady state and the power supplied for sample 7 at 51 °C. The slope of the fitting equation is for calculating the thermal conductivity if other parameters are known, as shown by the equation $\Delta R/Q = L\eta/(12\,kA)$.

will be mostly accumulated on the side facing the iridium target and it is reasonable to evaluate its cross-sectional area as $D\delta$, where D is the diameter of the nanowire and δ is the thickness of the iridium coating. Therefore the overall cross-sectional area is $(A + D\delta)$, including the influence of the iridium coating. The new effective thermal conductivity is then expressed as $k = QL\eta/[12(A + D\delta)\Delta R]$, and the value is determined as 3.9 W m^{-1} K^{-1}, slightly lower than the value without considering the thickness of the iridium film. This strategy will be used consistently with all samples to ensure that more accurate and effective thermophysical properties are determined for further analysis.

As mentioned before, in order to enhance the electrical conducting behavior an iridium thin film is coated over the nanowire surface, to ensure that the sample conducts electrical current. The generated Joule heat transfers along the axial direction so that the thermal properties can be measured. When the heat flows in the coating layer and TiO$_2$ nanowire along the axial direction, the effective thermal conductivity of the whole sample can be expressed as

$$k_{\text{eff}} = \frac{k_{\text{w}}A_2 + k_{\text{f}}A_{\text{f}}}{A_{\text{w}} + A_{\text{f}}}, \tag{5}$$

where k is the thermal conductivity and A is the cross-sectional area, while the subscripts w and f indicate the bare TiO$_2$ nanowire and the iridium film coating, respectively. An assumption is made to simplify the equation so that the cross-sectional area of the bare TiO$_2$ nanowire is much greater than that of the iridium film, which implies $A_{\text{w}} > A_{\text{f}}$. Meanwhile, according to the definition of the Lorenz number, k_{f} is expressed as

$$k_{\text{f}} = \frac{L_{\text{lorenz}}TL}{RA_{\text{f}}}. \tag{6}$$

Combining equations (5) and (6), we can determine the intrinsic thermal conductivity of bare TiO$_2$ nanowire as

$$k_{\text{w}} = k_{\text{eff}} - \frac{L_{\text{lorenz}}TL}{RA_{\text{w}}}. \tag{7}$$

The Lorenz number for iridium is chosen to be 2.5×10^{-8} W Ω K^{-2} [54], which is experimentally confirmed to have negligible variation within the temperature range of 300–373 K, and consequently is treated as a constant in this experiment [55]. Using the temperature and resistance at steady state, the calculated intrinsic thermal conductivity of sample 7 is 2.9 W m^{-1} K^{-1}, indicating that the effect from the iridium coating is about 25%. Compared with previous measurements of microscale or sub-microscale material, this effect from the iridium coating is relatively large because TiO$_2$ nanowire is only hundreds of nanometers thick and its surface is rough, based on the SEM images. The iridium coating must reach a certain thickness to form a fine film. In addition, the induced resistance of the sample must be controlled within a reasonable range for a balance between obtaining a strong enough signal and including as few unnecessary effects as possible. Therefore the effect from an iridium coating is higher than that from gold coatings reported before [49].

The same strategy is also applied to calculate the intrinsic thermal diffusivity of bare TiO$_2$ nanowire after the effective volume-based specific heat is obtained as $C_{\text{eff}} = \rho c_p = k_{\text{eff}}/a_{\text{eff}}$. Then the intrinsic thermal diffusivity is expressed as

$$a_{\text{w}} = a_{\text{eff}} - \frac{L_{\text{lorenz}}TL}{RA_{\text{w}}C_{\text{eff}}}. \tag{8}$$

From the intrinsic thermal conductivity, intrinsic thermal diffusivity and known specific heat [56] of bare TiO$_2$ nanowire, the density of sample 7 is calculated to be 2565 kg m^{-3}, lower than the reported bulk value of 3890 kg m^{-3} [53], supporting the speculation that defects and vacancies are created when the PVP content decomposes and the crystalline structure converts from amorphous to anatase during the calcination, leading to lower density than the bulk value. With the other parameters, the intrinsic thermal diffusivity of sample 7 is modified to 1.7×10^{-6} m^2 s^{-1}. Compared with the effective value of 2.1×10^{-6} m^2 s^{-1}, the estimation of the effect from the iridium coating is about 23%, close to the 25% from thermal conductivity modification. The parameters contained in these equations bring in uncertainty and the error propagation will be discussed in section 3.3 to examine the accuracy of the techniques in this work.

3.3. The thermal conductivity, thermal diffusivity and density of TiO$_2$ nanowires

In table 1, the dimensional parameters, experimental variables and calculated results are all presented along with the experimental uncertainties. The diameters of all the measured nanowires are from 250 to 400 nm, and the SEM images in figures 1(d) and 2 indicate that the uniformity of diameter is good. Meanwhile, although the magnification of the SEM image is as high as 300 000×, the blurry edges of the nanowires cause uncertainty in determining the diameters. The applied current in this work is controlled to be around tens of μA to ensure that the sample structure remains intact under Joule heating. The temperature coefficient of resistance varies from 1.38 to 17.3 Ω K^{-1} and the slopes of the resistance–power curves are mostly around 2–$4 \times$

Table 1. Experimental data and calculated results for all samples.

No.	Length (mm)	Diameter (nm)	DC current (µA)	$\Delta R/\Delta T$ (Ω K^{-1})	$\Delta R/\Delta Q$ ($\times 10^8$ Ω W^{-1})	Density (kg m^{-3})	Thermal diffusivity ($\times 10^{-6}$ m^2 s^{-1})	Thermal conductivity (W m^{-1} K^{-1})	Porosity (%)
1	0.13	250 ± 13	18.0	5.30	2.83	1430 ± 180	1.3 ± 0.2	1.3 ± 0.2	63
2	0.11	370 ± 19	26.0	8.30	2.11	1620 ± 200	1.9 ± 0.2	2.1 ± 0.4	58
3	0.11	295 ± 15	20.0	10.6	2.03	1960 ± 240	4.2 ± 0.5	5.6 ± 0.9	50
4	0.11	383 ± 19	30.0	2.05	0.239	1550 ± 190	4.6 ± 0.5	4.9 ± 0.8	60
5	0.11	320 ± 16	16.0	13.1	4.48	2190 ± 270	1.5 ± 0.2	2.3 ± 0.4	44
6	0.11	340 ± 17	14.0	17.3	4.21	2300 ± 280	2.1 ± 0.2	3.4 ± 0.6	41
7	0.11	342 ± 17	18.0	12.4	3.08	2570 ± 310	1.7 ± 0.2	2.9 ± 0.5	34
8	0.11	360 ± 18	35.0	1.38	0.212	3180 ± 390	1.5 ± 0.2	3.2 ± 0.5	18

10^8 Ω W^{-1} except for two samples. The thermal properties and densities in this table are intrinsic values excluding the impact from the iridium coating and are lower than the literature values of anatase TiO$_2$ crystal [52, 53]. As seen in the SEM image in figure 2 and also in other publications [27, 29, 31], the wavy and uneven surface structure to some extent demonstrates that the fabricated TiO$_2$ nanowire features relatively irregular and secondary porous features compared with bulk material. These irregularities and vacancies are mostly generated from the removal of PVP content during which the degradation may distort the fibrous matrix and also from the aggregation of TiO$_2$ particles in the crystalline structure transition procedure. Using the densities, estimates of the porosities of the nanowires are also concluded to be from about 18% to 63%, indicating that the calcination not only leaves structural distortions but also remarkable vacancies, which are possibly controllable if the experimental parameters are carefully selected [27].

The trends on how the thermal properties vary with density are presented in figure 6. When the density increases from 1434 to 3183 kg m^{-3}, the thermal conductivity shows a distinct increasing trend. Except for two obviously abnormal points that are higher than 4 W m^{-1} K^{-1}, the other data points display thermal conductivity increases with increasing density and these thermal conductivity values are lower than the literature value of 8.5 W m^{-1} K^{-1} for the bulk material [52]. As discussed before, the possible reason for this difference is because the interior structure distortions and vacancies from calcination induce phonon-impurity/defect scattering during their transport and, thus, lower the thermal conductivity. Additionally, the intrinsic thermal conductivities of single TiO$_2$ nanowires have been estimated qualitatively in our work before [49] and the results were in the range of 5–12 W m^{-1} K^{-1}, which are slightly greater than the values in this work but still consistent considering the simplifications made in that model and also the existence of secondary porous structures. The thermal diffusivity exhibits a flat trend against density. Within the range where the density increases, the thermal diffusivity changes from 1.3 × 10^{-6} to 2.1 × 10^{-6} m^2 s^{-1}, which is only about a 40% fluctuation and is much smaller than the thermal conductivity change. Two exceptional points are still plotted and their irregular values might be induced by strong measurement perturbation. With higher density, although the ability of the nanowire to conduct heat is improved, the more condensed structure also reinforces
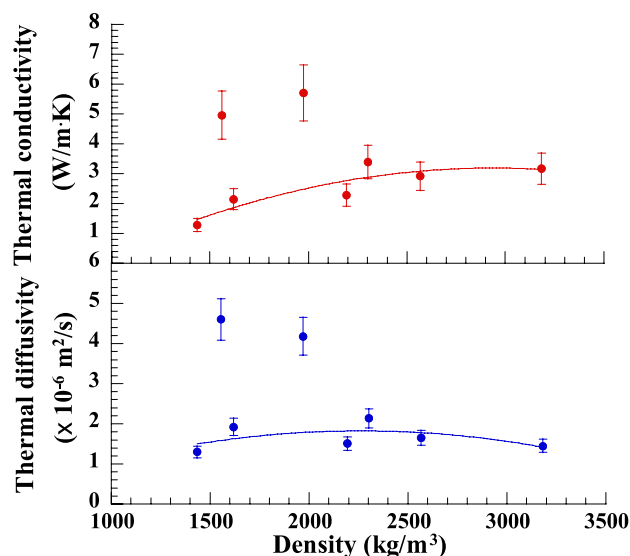
Figure 6. The thermal conductivities and thermal diffusivities of single TiO$_2$ nanowires versus density for all the samples listed in table 1. The curves are to guide the eyes to follow the data trend, with an error bar marked on each data point.

its capability to store heat. The comprehensive outcome is that no significant visible tendency is observed with thermal diffusivity, because the enhancements of both the capability to store heat and the ability to conduct heat are comparable.

The diameter of a nanowire (a very typical characteristic size) is another perspective from which to understand the thermal properties of small scale materials. In figure 7 a distinct trend is observed between density and diameter. When the diameter increases from 250 to 380 nm, the density also demonstrates a consistently ascending profile from 1434 to 3183 kg m^{-3}, except for a few discrepancies. These discrepancies may come from unexpected conditional perturbation during the experiment and dimension measurement uncertainties. This visible trend is largely caused by the crystal structure transition to a large cluster during calcination. Larger diameters feature more aggregated anatase crystal clusters and consequently give lower portions of vacancies. Accordingly the densities show larger values. For the thermal transport properties, the variation in the range of diameters is not large enough to impose substantial impact on the thermal diffusivity when the diameter changes from 250 to 380 nm, while it is evident

that this tendency is observed for the thermal conductivity. For the thermal diffusivity, when the diameter increases, only a variation of around $1–2 \times 10^{-6}$ m^2 s^{-1} is observed and it is roughly a flat trend. However, as an intrinsic property that does receive significant influence from the crystal structure and imperfections, the thermal conductivity presents stronger responses to diameter variations. As seen in figure 7, when the diameter increases from 250 to 370 nm, the thermal conductivity strongly increases from 1.3 to 4.9 W m^{-1} K^{-1}. This profile is still accompanied by strong fluctuations. The main explanation for the increasing trend is that a larger diameter is roughly connected to a lower porosity, and therefore fewer vacancies or holes exist as an impediment to phonon transfer. Another possible reason is that large nanowire diameters decrease the probability of phonon–surface scattering and consequently give higher thermal conductivities. Predictions can be made that if the diameter increases by more than one order of magnitude, the thermal conductivity would be affected much more significantly. As discussed before, because of the extremely small scale, dimensional measurements and experimental conditions can both influence the experimental uncertainty and they are the main reasons why certain anomalous points stand out. First, when measuring the diameter, the magnification of the SEM image was increased to 300 000×. Under this huge magnification, the edge of the nanowire was not sharp enough for precise measurement and the blurry character causes reading errors to a certain degree. Second, although the samples were fabricated and processed in the same way, the degree of environmental perturbation varies from sample to sample. After obtaining valid data for analysis, a few points appear with irregular values compared with the majority. These points are not considered wrong but less accurate because they may have received a relatively stronger impact from experimental pertubations. They are still plotted out for analysis purposes. Additionally, no matter how accurate the data are, uncertainties are inevitable in the measurements and calculations.

3.4. Uncertainty analysis

The thermal diffusivity is obtained by fitting different values until the profile with the smallest fitting error is acquired. During the fitting procedure, it is reasonable to acquire the fitting uncertainty by changing the values to observe how strong the deviation is from the experimental profile. When the value is varied over ±8%, the corresponding profiles show strong deviation from the experimental curve and therefore the uncertainty from the data fitting is 8%, as displayed in figure 4(b). With the high-magnification SEM image, the length measurement uncertainty is as small as 1% and therefore the L^2 term brings in about a 2% uncertainty. Thus the total uncertainty for the thermal diffusivity is about 8.3%.

Calculation of the thermal conductivity is more complicated as stated in previous discussion. The uncertainty of the resistance is estimated to be 5%. Therefore, the uncertainty of the temperature coefficient of the resistance is about 5.1%, mostly from the resistance. The uncertainty of the power
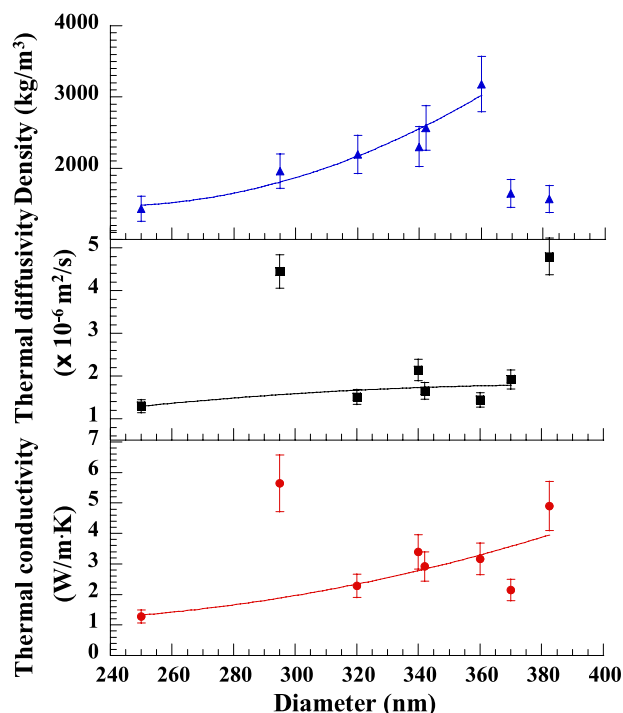
Figure 7. The thermal conductivity, thermal diffusivity and density versus the diameter for all measured TiO$_2$ nanowires, with lines to guide the eyes to the data trend. An error bar is shown for each data point.

is around 1%. The measurement of the diameter is based on a high-magnification image and is found to have a 5% uncertainty because of the difficulty of adjusting the focus. Consequently, the total uncertainty for the effective thermal conductivity is about 9%. The uncertainty of the effective volume-based specific heat is also calculated to be 12.24% based on the discussion above.

The overall uncertainty of the intrinsic thermal diffusivity is 11.7%. Following the same method, the uncertainty of the intrinsic thermal conductivity is calculated to be 16.5%. From the uncertainty analysis, it is conclusive that the uncertainties of major parameters and results in this experiment are controlled within acceptable ranges, considering the differences among samples and varying experimental conditions. The uncertainties are listed in table 1, as supplements to the measurement values, along with error bars marked in the figures for each discrete data point.

4. Conclusion

In this paper, single TiO$_2$ nanowires, which are considered to be the intrinsic units composing TiO$_2$ nanofilm and nanowire arrays, were exclusively studied. Highly oriented TiO$_2$ nanowires were first fabricated using the electrospinning technique and collected on a pre-processed TEM grid. After hydrolysis and calcination, only one TiO$_2$ nanowire was chosen for thermal characterization. Raman spectra confirmed the anatase polymorph of the single TiO$_2$ nanowire. In calcination, both decomposition of the PVP content and the transition of the TiO$_2$ crystalline structure occurred. These

processes strongly distorted the fibrous structure and induced obvious aggregation of the TiO$_2$ particles, consequently resulting in a secondary porous structure. The porosity was further evaluated by the results from thermal characterization. Via TET characterization, the obtained thermal conductivity varied from 1.3 to 5.6 W m^{-1} K^{-1} while the density changed from 1430 to 3180 kg m^{-3}, significantly lower than the bulk value because the structural distortions and imperfections strongly hampered the phonon transport. With increasing density, the thermal conductivity presented an increasing tendency while the thermal diffusivity simply scattered around a certain value, showing a flat trend. For all the samples in this work, the high porosity varied from 18% to 63%, showing that the crystal structure contained substantial vacancies and spacing. The diameter of the nanowire was also investigated to understand its relationship with the thermal properties. The range of the diameter was from 250 to 380 nm. Within this small variation, the thermal conductivity showed a distinct trend with a certain fluctuation. The density changed more strongly with the diameter, indicating that when the diameter varies, the levels of vacancies and irregularity may be affected significantly.

Acknowledgments

References

[1] Xia Y N, Yang P D, Sun Y G, Wu Y Y, Mayers B, Gates B, Yin Y D, Kim F and Yan Y Q 2003 One-dimensional nanostructures: synthesis, characterization, and applications *Adv. Mater.* **15** 353–89

[2] Hu J T, Odom T W and Lieber C M 1999 Chemistry and physics in one dimension: synthesis and properties of nanowires and nanotubes *Acc. Chem. Res.* **32** 435–45

[3] Melendres C A, Narayanasamy A, Maroni V A and Siegel R W 1989 Raman-spectroscopy of nanophase TiO$_2$ *J. Mater. Res.* **4** 1246–50

[4] Terwilliger C D and Chiang Y M 1993 Excess thermodynamic properties of nanophase titanium-dioxide prepared by chemical and physical methods *Mater. Res. S* C **286** 15–20

[5] Matsuda S 1983 Titanium-oxide based catalysts—a review *Appl. Catal.* **8** 149–65

[6] Dagan G and Tomkiewicz M 1993 TiO$_2$ aerogels for photocatalytic decontamination of aquatic environments *J. Phys. Chem.* **97** 12651–5

[7] Azad A M, Akbar S A, Younkman L B and Alim M A 1994 High-temperature immittance response in anatase-based sensor materials *J. Am. Ceram. Soc.* **77** 3145–52

[8] Azad A M, Younkman L B, Akbar S A and Alim M A 1994 Characterization of TiO$_2$-based sensor materials using immittance spectroscopy *J. Am. Ceram. Soc.* **77** 481–6

[9] Bach U, Lupo D, Comte P, Moser J E, Weissortel F, Salbeck J, Spreitzer H and Gratzel M 1998 Solid-state dye-sensitized mesoporous TiO$_2$ solar cells with high photon-to-electron conversion efficiencies *Nature* **395** 583–5

[10] Gratzel M 2001 Photoelectrochemical cells *Nature* **414** 338–44

[11] Lei Y, Zhang L D, Meng G W, Li G H, Zhang X Y, Liang C H, Chen W and Wang S X 2001 Preparation and photoluminescence of highly ordered TiO$_2$ nanowire arrays *Appl. Phys. Lett.* **78** 1125–7

[12] Lin Y, Wu G S, Yuan X Y, Xie T and Zhang L D 2003 Fabrication and optical properties of TiO$_2$ nanowire arrays made by sol–gel electrophoresis deposition into anodic alumina membranes *J. Phys.: Condens. Matter* **15** 2917–22

[13] Miao L, Tanemura S, Toh S, Kaneko K and Tanemura M 2004 Heating-sol–gel template process for the growth of TiO$_2$ nanorods with rutile and anatase structure *Appl. Surf. Sci.* **238** 175–9

[14] Miao L, Tanemura S, Toh S, Kaneko K and Tanemura M 2004 Fabrication, characterization and raman study of anatase TiO$_2$ nanorods by a heating-sol–gel template process *J. Cryst. Growth* **264** 246–52

[15] Yuan Z Y and Su B L 2004 Titanium oxide nanotubes, nanofibers and nanowires *Colloid Surf.* A **241** 173–83

[16] Francioso L and Siciliano P 2006 Top-down contact lithography fabrication of a TiO$_2$ nanowire array over a SiO$_2$ mesa *Nanotechnology* **17** 3761–7

[17] Kolen'ko Y V, Kovnir K A, Gavrilov A I, Garshev A V, Frantti J, Lebedev O I, Churagulov B R, Van Tendeloo G and Yoshimura M 2006 Hydrothermal synthesis and characterization of nanorods of various titanates and titanium dioxide *J. Phys. Chem.* B **110** 4030–8

[18] Zhang X W, Pan J H, Du A J, Fu W J, Sun D D and Leckie J O 2009 Combination of one-dimensional TiO$_2$ nanowire photocatalytic oxidation with microfiltration for water treatment *Water Res.* **43** 1179–86

[19] Ge Z X, Wei A X, Liu J, Zhao W and Liu C B 2010 Synthesis and photovoltaic devices performance of single crystalline TiO$_2$ nanowire bundle arrays *J. Inorg. Mater.* **25** 1105–9

[20] Liao J Y, Lei B X, Wang Y F, Liu J M, Su C Y and Kuang D B 2011 Hydrothermal fabrication of quasi-one-dimensional single-crystalline anatase TiO$_2$ nanostructures on FTO glass and their applications in dye-sensitized solar cells *Chem.—Eur. J.* **17** 1352–7

[21] Xu Y, Gu H S, Xia H T and Hu M Z 2011 TiO$_2$ nanowire dye-sensitized solar cells fabricated by hydrothermal method *3rd Int. Photonics and Optoelectronics Mtg (Poem 2010)* vol 276 p 012196

[22] Lei Y, Zhang L D and Fan J C 2001 Fabrication, characterization and raman study of TiO$_2$ nanowire arrays prepared by anodic oxidative hydrolysis of TiCl$_3$ *Chem. Phys. Lett.* **338** 231–6

[23] Zhang X Y, Yao B D, Zhao L X, Liang C H, Zhang L D and Mao Y Q 2001 Electrochemical fabrication of single-crystalline anatase TiO$_2$ nanowire arrays *J. Electrochem. Soc.* **148** G398–400

[24] Jiao Z, Wu M H, Shi L Y, Li Z and Wang Y L 2004 Preparation of TiO$_2$ nanowire by atomic force microscopy electrochemical anode oxidation *Chin. J. Inorg. Chem.* **20** 1325–8

[25] Liu S Q and Huang K L 2005 Straightforward fabrication of highly ordered TiO$_2$ nanowire arrays in AAM on aluminum substrate *Sol. Energy Mater. Sol. Cells* **85** 125–31

[26] Cai F G, Yang F, Zhao Y and Cheng C H 2011 Preparation of TiO$_2$ nanotube and nanotube/nanowire composite arrays by temperature control *Chin. J. Inorg. Chem.* **27** 504–8

[27] Li D and Xia Y N 2003 Fabrication of titania nanofibers by electrospinning *Nano Lett.* **3** 555–60

[28] Subbiah T, Bhat G S, Tock R W, Pararneswaran S and Ramkumar S S 2005 Electrospinning of nanofibers *J. Appl. Polym. Sci.* **96** 557–69

[29] Son W K, Cho D and Park W H 2006 Direct electrospinning of ultrafine titania fibres in the absence of polymer additives

and formation of pure anatase titania fibres at low temperature *Nanotechnology* **17** 439–43

[30] Tekmen C, Suslu A and Cocen U 2008 Titania nanofibers prepared by electrospinning *Mater. Lett.* **62** 4470–2

[31] Zhao J G, Jia C W, Duan H G, Li H and Xie E Q 2008 Structural properties and photoluminescence of TiO$_2$ nanofibers were fabricated by electrospinning *J. Alloys Compounds* **461** 447–50

[32] Chung Y A, Lee C Y, Peng C W and Chiu H T 2006 Reactive template assisted growth of one-dimensional nanostructures of titanium dioxide *Mater. Chem. Phys.* **100** 380–4

[33] Venkataramanan N S, Matsui K, Kawanami H and Ikushima Y 2007 Green synthesis of titania nanowire composites on natural cellulose fibers *Green Chem.* **9** 18–9

[34] Baik J M, Kim M H, Larson C, Chen X H, Guo S J, Wodtke A M and Moskovits M 2008 High-yield TiO$_2$ nanowire synthesis and single nanowire field-effect transistor fabrication *Appl. Phys. Lett.* **92** 242111

[35] Kim J I, Lee S Y and Pyun J C 2009 Characterization of photocatalytic activity of TiO$_2$ nanowire synthesized from Ti-plate by wet corrosion process *Curr. Appl. Phys.* **9** E252–5

[36] Park J, Ryu Y, Kim H and Yu C 2009 Simple and fast annealing synthesis of titanium dioxide nanostructures and morphology transformation during annealing processes *Nanotechnology* **20** 105608

[37] Inoue Y, Noda I, Torikai T, Watari T, Hotokebuchi T and Yada M 2010 TiO$_2$ nanotube, nanowire, and rhomboid-shaped particle thin films fixed on a titanium metal plate *J. Solid State Chem.* **183** 57–64

[38] Kim M H, Baik J M, Zhang J P, Larson C, Li Y L, Stucky G D, Moskovits M and Wodtke A M 2010 TiO$_2$ nanowire growth driven by phosphorus-doped nanocatalysis *J. Phys. Chem.* C **114** 10697–702

[39] Sedach P A, Gordon T J, Sayed S Y, Furstenhaupt T, Sui R H, Baumgartner T and Berlinguette C P 2010 Solution growth of anatase TiO$_2$ nanowires from transparent conducting glass substrates *J. Mater. Chem.* **20** 5063–9

[40] Wakaya F, Miki M, Fukuyama C, Murakami K, Abo S and Takai M 2010 Fabrication and electron field-emission properties of titanium oxide nanowire on glass substrate *J. Vac. Sci. Technol.* B **28** C2b24–6

[41] Yu C and Park J 2010 Thermal annealing synthesis of titanium-dioxide nanowire–nanoparticle hetero-structures *J. Solid State Chem.* **183** 2268–73

[42] Chen X and Mao S S 2007 Titanium dioxide nanomaterials: synthesis, properties, modifications, and applications *Chem. Rev.* **107** 2891–959

[43] Berman R, Foster E L and Ziman J M 1956 The thermal conductivity of dielectric crystals—the effect of isotopes *Proc. R. Soc.* A **237** 344–54

[44] Beppu T, Yamaguchi S and Hayase S 2007 Improvement of heat resistant properties of TiO$_2$ nanowires and application to dye-sensitized solar cells *Japan. J. Appl. Phys.* **46** 4307–11

[45] Lambropoulos J C, Jolly M R, Amsden C A, Gilman S E, Sinicropi M J, Diakomihalis D and Jacobs S D 1989 Thermal-conductivity of dielectric thin-films *J. Appl. Phys.* **66** 4230–42

[46] Wu Z L, Reichling M, Hu X Q, Balasubramanian K and Guenther K H 1993 Absorption and thermal-conductivity of oxide thin-films measured by photothermal displacement and reflectance methods *Appl. Opt.* **32** 5660–5

[47] Lee S M, Cahill D G and Allen T H 1995 Thermal-conductivity of sputtered oxide-films *Phys. Rev.* B **52** 253–7

[48] Guo J Q, Wang X W and Wang T 2007 Thermal characterization of microscale conductive and nonconductive wires using transient electrothermal technique *J. Appl. Phys.* **101** 063537

[49] Feng X, Wang X, Chen X and Yue Y 2011 Thermo-physical properties of thin films composed of anatase TiO$_2$ nanofibers *Acta Mater.* **59** 1934–44

[50] Li D, Wang Y L and Xia Y N 2003 Electrospinning of polymeric and ceramic nanofibers as uniaxially aligned arrays *Nano Lett.* **3** 1167–71

[51] Ohsaka T, Izumi F and Fujiki Y 1978 Raman-spectrum of anatase, TiO$_2$ *J. Raman Spectrosc.* **7** 321–4

[52] Touloukian Y S P, W R, Ho C Y and Klemens P G 1970 *Thermophyiscal Properties of Matter-Thermal Conductivity of Non-Metallic Solids* vol 2 (New York: IFI/Plenum)

[53] Guo L Y, Wang X W, Wang J, Lin Z Q and Gacek S 2009 Anisotropic thermal transport in highly ordered TiO$_2$ nanotube arrays *J. Appl. Phys.* **106** 123526

[54] Kumar G S, Prasad G and Pohl R O 1993 Experimental determinations of the lorenz number *J. Mater. Sci.* **28** 4261–72

[55] Powell R W, Tye R P and Woodman M J 1962 Thermal conductivities and electrical resistivities of the platinum metals *Platinum Met. Rev.* **6** 138–43

[56] Smith S J, Stevens R, Liu S F, Li G S, Navrotsky A, Boerio-Goates J and Woodfield B F 2009 Heat capacities and thermodynamic functions of TiO$_2$ anatase and rutile: analysis of phase stability *Am. Mineral.* **94** 236–43

[57] Huang X P, Wang J M, Eres G and Wang X W 2011 Thermophysical properties of multi-wall carbon nanotube bundles at elevated temperatures up to 830 K *Carbon* **49** 1680–91

[58] Fang J, Reitz C, Brezesinski T, Nemanick E J, Kang C B, Tolber S H and Pilon L 2011 Thermal conductivity of highly-ordered mesoporous titania thin films from 30 to 320 K *J. Phys. Chem.* C **115** 14606–14